Membrane-wrapped nanoparticles probe divergent roles of GM3 and phosphatidylserine in lipid-mediated viral entry pathways

Fangda Xu[a,b], Asanga Bandara[a], Hisashi Akiyama[c], Behnaz Eshaghi[a,b], David Stelter[a], Tom Keyes[a], John E. Straub[a], Suryaram Gummuluru[c,1], and Björn M. Reinhard[a,b,1]

[a]Department of Chemistry, Boston University, Boston, MA 02215; [b]The Photonics Center, Boston University, Boston, MA 02215; and [c]Department of Microbiology, School of Medicine, Boston University, Boston, MA 02215

Gold nanoparticles (NPs) wrapped in a membrane can be utilized as artificial virus nanoparticles (AVNs) that combine the large nonblinking or bleaching optical cross-section of the NP core with the biological surface properties and functionalities provided by a self-assembled lipid membrane. We used these hybrid nanomaterials to test the roles of monosialodihexosylganglioside (GM3) and phosphatidylserine (PS) for a lipid-mediated targeting of virus-containing compartments (VCCs) in macrophages. GM3-presenting AVNs bind to CD169 (Siglec-1)–expressing macrophages, but inclusion of PS in the GM3-containing AVN membrane decreases binding. Molecular dynamics simulations of the AVN membrane and experimental binding studies of CD169 to GM3-presenting AVNs reveal Na$^+$-mediated interactions between GM3 and PS as a potential cause of the antagonistic action on binding by the two negatively charged lipids. GM3-functionalized AVNs with no or low PS content localize to tetherin$^+$, CD9$^+$ VCC in a membrane composition-depending fashion, but increasing amounts of PS in the AVN membrane redirect the NP to lysosomal compartments. Interestingly, this compartmentalization is highly GM3 specific. Even AVNs presenting the related monosialotetrahexosylganglioside (GM1) fail to achieve an accumulation in VCC. AVN localization to VCC was observed for AVN with gold NP core but not for liposomes, suggesting that NP sequestration into VCC has additional requirements beyond ligand (GM3)–receptor (CD169) recognition that are related to the physical properties of the NP core. Our results confirm AVN as a scalable platform for elucidating the mechanisms of lipid-mediated viral entry pathways and for selective intracellular targeting.

bioplasmonics | HIV-1 | glycolipids | apoptotic mimicry | virus-containing compartments

Viruses are smart nanoparticles (NPs) that have evolved, as in the case of HIV (HIV-1), to exploit endogenous cell recognition mechanisms to target specific host cells. Understanding and recapitulating these functionalities are not only of significant interest from virological and translational standpoints but also, have additional relevance in nanomedicine for developing enhanced biomimetic NP-based delivery and therapy strategies. HIV-1 is an enveloped virus that obtains its membrane from the host cell during budding. Since some of the host cell-derived viral envelope lipids are recognized by cellular receptors that trigger subsequent uptake, lipid-based entry factors in the viral membrane can complement the function of virus-encoded membrane glycoproteins in targeting host cells and initiating uptake. In particular, phosphatidylserine (PS) and monosialodihexosylganglioside (GM3) are two lipids with functional roles in HIV-1 infection. PS contained in the viral envelope is a cofactor in the infection of monocytic cells by HIV-1 (1). By presenting PS on its surface, a virus particle imitates apoptotic cellular debris. In a process commonly referred to as viral apoptotic mimicry (2), HIV-1 and other viruses (3, 4), including Ebola, are thought to enhance host cell binding, infection, and replication by parasitizing apoptotic debris clearance and antiinflammatory mechanisms. PS-mediated virus uptake occurs pri-

marily via clathrin-mediated endocytosis or macropinocytosis and links to an endocytotic pathway (5). Similar to PS, it has been suggested that the role of GM3 in viral infectivity derives from an evolutionary adaption of endogenous cellular behavior: in particular, exosome-based intercell communication (6). The ganglioside GM3 binds to the sialic acid-recognizing lectin CD169 (Siglec-1), which is expressed by myeloid cells, such as macrophages and dendritic cells (7–9). Intriguingly, GM3-CD169–mediated binding of NP to mature monocyte-derived dendritic cells (MDDCs) triggers a unique compartmentalization of NP in peripheral non-endolysosomal membrane compartments that attract surface-scanning T cells (10, 11). Together, these observations suggest that key steps in HIV-1 transinfection, a process in which virus is transmitted to T-cell targets via dendritic cells or macrophages, are driven by GM3-CD169 recognition and can occur in a viral glycoprotein-independent fashion (12). Consistent with this model, the ganglioside receptor CD169 orchestrates the accumulation of exogenous virus particles in apparently intracellular compartments, so-called virus-containing compartments (VCCs) in macrophages and mature MDDCs (12, 13). With their unique structure and nonendolysosomal nature, VCCs are considered an ideal reservoir for the virus to evade the host's immune system (14–16) and form a

---

Significance

Membrane-wrapped noble metal nanoparticles provide a synthetic platform to investigate lipid-mediated, glycoprotein-independent virus–cell interactions. Different from membrane-wrapped virus-like particles (VLPs), these artificial virus nanoparticles (AVNs) are not derived from cellular systems and can contain organic or inorganic cores optimized for imaging or delivery purposes. A particular advantage is the rational control over the AVN membrane composition, which can be complex or undefined in VLP. This work shows that monosialodihexosylganglioside-presenting AVNs accumulate in virus-containing compartments (VCCs) that represent assembly sites for HIV-1. VCCs provide evasion for HIV-1 from the immune system as well as antiviral therapeutics. The ability to target VCCs with AVNs provides opportunities for eradicating a putative reservoir of HIV-1 persistence.

---

major obstacle for the eradication of HIV-1 with conventional combination antiretroviral therapy, either due to long-term preservation of infectious virus particles or due to decreased efficiency of antiretrovirals to inhibit cell-associated HIV transmission (17, 18).

In the case of HIV-1 infection, both GM3 and PS are enriched in lipid rafts, from which the virus preferentially buds (19). Consequently, both lipids are enriched in the viral envelope membrane and are available to interact with their respective receptors. It is currently unclear if and how PS and GM3 interact to target the viral glycoprotein-independent entry pathway that can result either in PS-mediated endocytosis/phagocytosis or in GM3-mediated collection in VCCs of macrophages. It cannot be excluded that the GM3/PS ratio in the viral membrane represents a regulatory mechanism to determine intracellular distributions and fates after glycoprotein-independent virus capture. A successful decoding of this lipid-controlled regulatory mechanism requires elucidating the rules that predict the intracellular fate of a virus with a given membrane composition and developing NP-based biomimetic drug delivery strategies (20–24) for selectively targeting VCC reservoirs in macrophages. Membrane-wrapped NPs (25–28) containing a self-assembled membrane of defined composition around an NP core represent synthetic models for enveloped virus particles. Furthermore, we have shown previously that membrane-wrapped NPs with a plasmonic NP core are artificial virus nanoparticles (AVNs) (11) that successfully recapitulate CD169-dependent HIV-1 uptake in MDDCs (10, 11, 29). In this work, we apply AVNs as an experimental platform to elucidate the interplay of PS and GM3 in triggering VCC formation in macrophages. We show that VCC localization specifically requires GM3-CD169 interactions and that other structurally related gangliosides, such as monosialotetrahexosylganglioside (GM1), fail to induce sequestration into VCC. The importance of the AVN core in VCC formation in macrophages is experimentally verified, which indicates that such AVN models could be developed further into a versatile platform to study the role of core stiffness in the early events of the HIV-1 infection cycle. We also compare the intracellular fate of AVN with different GM3/PS ratios with HIV-1 virus-like particles (VLPs) and Ebola VLPs. We show that GM3-presenting AVNs with low PS concentration are sequestered together with HIV VLPs in VCC, while AVNs with high PS concentration are collected with Ebola VLPs in lysosomes. These findings suggest that membrane lipid composition, a crucial determinant of enveloped virus entry and trafficking, can be exploited to achieve selective intracellular targeting of NPs.

Results

The AVN design used in this work (11, 25, 29–31) is outlined in Fig. 1A. A membrane was self-assembled from known lipid components [1,2-dipalmitoyl-sn-glycero-3-phosphocholine (DPPC), 1,2-dioleoyl-sn-glycero-3-phospho-L-serine (DOPS), cholesterol, GM3] in predetermined ratios around a central gold NP core. The membrane assembly under well-defined conditions provides a rational strategy for controlling the relative PS/GM3 content in the membrane, while the gold core provides a large resonant optical cross-section for easy detection in dark-field microscopy (32–36). The size of the gold core was ~90 nm, resulting in a total AVN size that is comparable with that of HIV-1 particles (11). Membrane wrapping of the NP was accomplished using a one-pot assembly strategy, in which liposomes and citrate-stabilized gold NPs were mixed in the presence of octadecanethiol (25, 31). Octadecanethiol binds readily to the NP and establishes a hydrophobic surface, onto which lipids from coincubated liposomes can anchor. Optical colocalization of the fluorescence signal of a lipid dye (0.1 mol % 16:0 lissamine rhodamine B 1,2-dioleoyl-sn-glycero-3-phosphoethanolamine) added during AVN assembly and dark-field scattering from the NP cores revealed

nearly 100% association (*SI Appendix*, Fig. S1), confirming the structural model of a membrane-wrapped NP. Due to the superb optical properties of the noble metal NP core, the interactions between AVNs and immunolabeled cellular components can be probed through optical colocalization. Another benefit of the AVN design is that the gold core facilitates a precise quantification of cellular uptake through inductively coupled MS (ICP-MS) (37). We focus in this study on the interplay of GM3 and PS in determining the intracellular fate of AVNs and prepared AVNs with five different GM3/PS mole percentage ratios within a physiological meaningful concentration range (20): 3/0, 3/2, 3/10, 0/3, and 0/10. Fig. 1B shows that the negative charge density of the AVN increases continuously as function of nominal PS concentration, confirming a successful integration of the negatively charged lipid in the membrane. Fig. 1B, *Inset* contains the relative ganglioside content (here GM1) in AVN as determined by ELISA for different PS contents. The ELISA intensities show no significant differences between the AVNs with different PS concentrations, suggesting that an increase in PS does not affect the ganglioside concentration in the membrane. Having in hand AVNs with a rationally tunable membrane composition, we set out to systematically investigate the impact of the GM3/PS ratio on uptake and intracellular fate. We chose CD169+ THP-1 macrophages constitutively expressing CD169 (38) [differentiated into macrophages upon phorbol myristate acetate (PMA) treatment] as a cell model in our studies. Macrophages express various PS receptors (39, 40), and CD169-expressing myeloid macrophages are known to be vectors of *cis* and *trans* HIV-1 infection (13, 41). Importantly, sinus-lining CD169+ macrophages have been shown to play a central role in retrovirus transinfection of lymphocytes in the lymph nodes (42). We validated CD169 expression in our THP-1 macrophage model through immunofluorescence. The representative image in Fig. 1C shows that CD169 is enriched in a rim around the basal membrane of surface-attached macrophages. CD169 recognizes GM3 presented on AVNs and facilitates ganglioside-mediated binding of membrane-wrapped NPs (10, 11). Control experiments with CD169+ and CD169− THP-1 cells (*SI Appendix*, Fig. S2) confirmed GM3-CD169–mediated binding for the macrophages investigated in this work. To characterize the effect of the GM3/PS ratio on AVN uptake, we incubated the macrophages with AVN at a ratio of 1,000:1 (particles:cell) for 45 min in serum-free buffer before quantifying the cellular gold content by ICP-MS (Fig. 2A). Interestingly, GM3 without PS (3/0) or high PS concentration without GM3 (0/10) led to a much higher AVN uptake than the equivalent combination of both GM3 and PS (3/10). This finding is intriguing, especially if one considers that the membrane of HIV-1 particles that bud from the host cell plasma membrane is enriched in both sphingolipids, including gangliosides, and PS (19).

To obtain additional insight into the mechanism of AVN uptake, we characterized the intracellular spatial distribution of AVN with different GM3/PS ratios and tested their colocalization with CD169. Fig. 2B shows representative images taken after 45 min of AVN incubation. For AVNs with a GM3/PS ratio of 3/0, we frequently observed a phenotype, *PH1*, in which the AVNs are confined to the CD169-enriched rim of the cell. If PS was added to the AVN membrane, the colocalization of AVN and CD169 deteriorated, and a second phenotype, *PH2*, containing AVN localized throughout the cytoplasm became more prominent with increasing PS content. Fig. 2C summarizes the observed frequency of *PH1* as a function of GM3/PS ratio in the presence of polyinosinic acid (poly-I). Poly-I blocks PS-mediated AVN binding to scavenger/pattern recognition receptors and facilitates a quantification of the effect that the GM3/PS ratio has on the CD169-dependent peripheral enrichment of AVN. Fig. 2C shows clearly that the contribution of *PH1* decreases with decreasing GM3/PS ratio. Although poly-I can block charge-mediated recognition of PS, it does not block specific PS
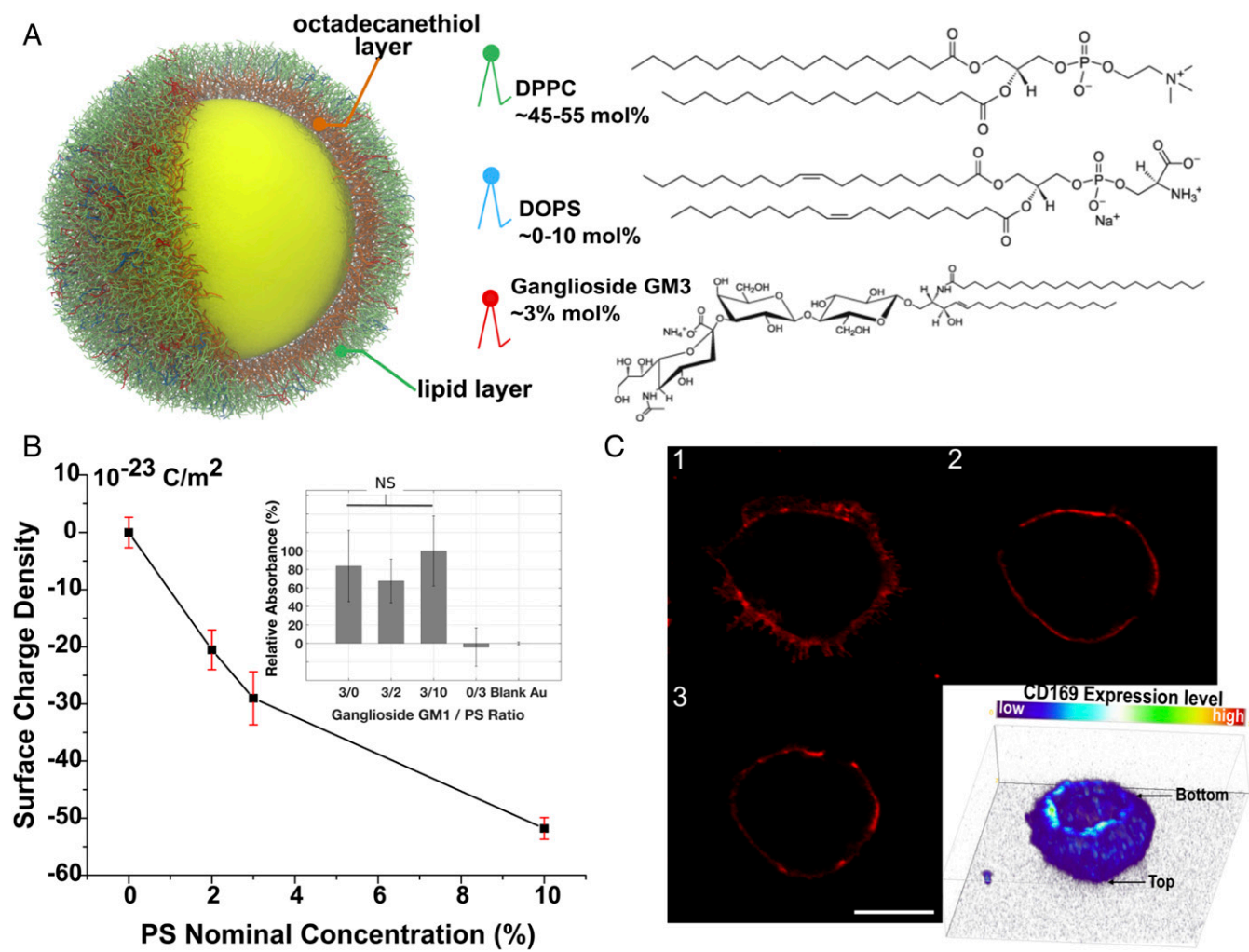
Fig. 1. AVN design and characterization. (*A*) Structural model of an AVN, which consists of a 90-nm Au NP core (yellow), an octadecanethiol inner membrane layer (orange), and a lipid membrane outer layer assembled from DPPC (green), DOPS (blue), GM3 (red), and cholesterol (not shown). The structure of the lipids and their mole percentage range are included. (*B*) Zeta potential and relative ganglioside (here GM1) loading determined by ELISA (*Inset*) as a function of AVN membrane composition. The plotted data are the average of at least three independent experiments per condition. (*C*) Three selected confocal sections at increasing (1–3) heights over the substrate and the complete 3D confocal reconstruction (*Inset*) show the surface distribution of CD169 in a THP-1/ PMA macrophage. Note that, to enhance CD169 visibility, the basal membrane is shown pointing up in the confocal reconstruction. NS, not significant.

recognition through PS receptors, such as TAM (43) or TIM (44) family receptors, which dominate at high PS concentrations. We conclude that AVNs with low PS concentration (e.g., 3/0 AVN) are uptaken by CD169-mediated cell–AVN interactions, whereas for higher PS concentrations (e.g., 3/10 AVN), NP uptake no longer exclusively depends on CD169 but is, instead, progressively dominated by PS receptors.

The coexistence of two competing uptake pathways that culminate in distinct phenotypes *PH1* and *PH2* does, however, not explain the observed antagonism between GM3 and PS, as orthogonal AVN recognition mechanisms should result in increased AVN uptake. One possible explanation for the experimentally observed behavior is direct interactions between colocalized GM3 and PS that perturb receptor recognition and/or subsequent uptake. To validate the feasibility of an association of PS and GM3, we performed molecular dynamics (MD) simulations of the lipid distributions in a conventional lipid membrane bilayer (Fig. 2 *D* and *E*). We included both coarse-grained (CG) and all-atom (AA) MD simulations. Despite differences in the details, which will be reported and analyzed elsewhere, both computational approaches confirm interactions between GM3 and PS. The radial

distribution functions and trajectory snapshots taken from the AA model reveal a spatial colocalization of GM3 and PS that is facilitated by Na$^+$ cations with concentration that is enriched near the lipid head group plane (Fig. 2 *D* and *E*). CG simulations reveal a prominent peak in the GM3-PS radial distributions, indicating strong colocalization, while the AA radial distributions in Fig. 2*D*, *Inset* show comparatively modest nonspecific interactions. These differences in the exact peak positions and widths of the radial distribution functions of GM3-PS and GM3-Na$^+$ in CG and AA MD simulations can be attributed to the extended timescales and system sizes achieved in the CG simulations and the accurate description of the electrostatics in general and more specifically, the hydrogen bonds and aqueous solvation of the lipid head group in the AA model (45). Schmalhorst et al. (46) have shown limitations and suggested improvements to the MARTINI CG model in relation to the CG polysaccharides; the apparent disparity between AA and CG results seen in this study illustrates the need for similar improvements to the glycolipids. Fig. 2*E* visualizes the GM3-PS colocalization with the Na$^+$ ions in the background, evident in the final configuration of the CG and AA simulations. In the next step, we experimentally tested the effect of Na$^+$ ions on
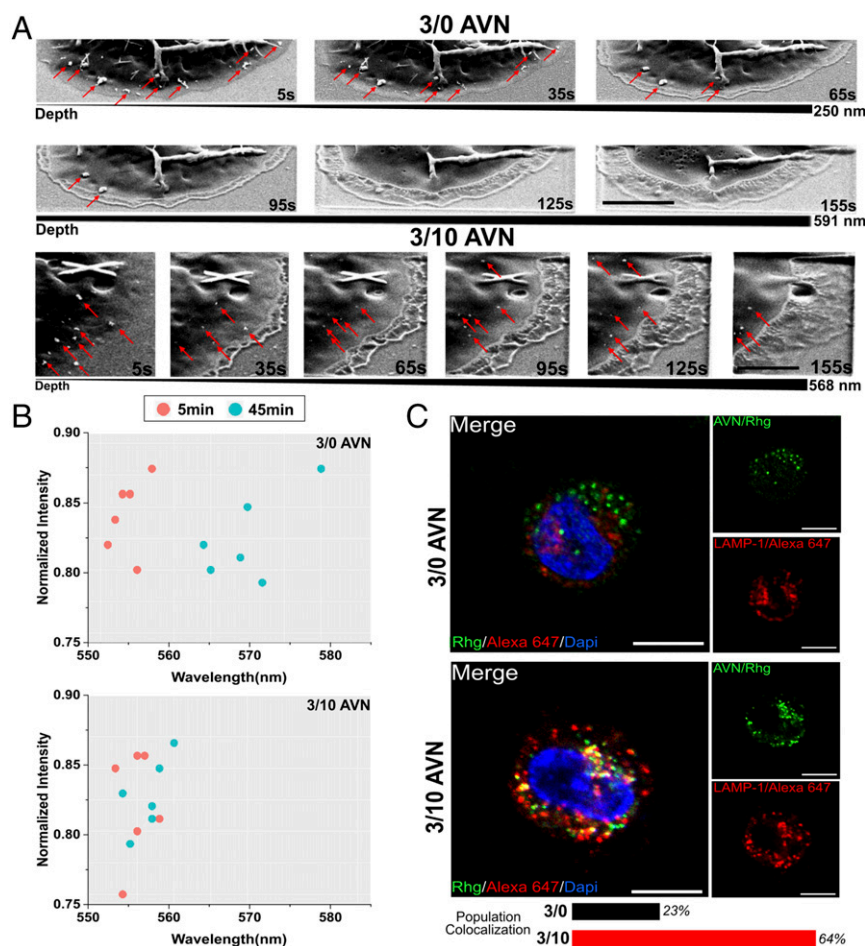
Fig. 2. Characterization of AVN binding and uptake in CD169^{+} THP-1 cells as a function the GM3/PS ratio. (*A*) Gold content per cell (parts per billion) as a function of the GM3/PS ratio determined by ICP-MS. The average of four independent experiments is plotted. ***$P < 0.001$ relative to 3/0 AVNs. (*B*) Wide-field images of AVNs containing CD169^{+} THP-1 cells for different GM3/PS ratios. CD169 and nucleus are costained. All images were acquired 45 min after AVN addition. (Scale bar: 5 μm.) (*C*) Relative frequency of *PH1* for AVN with GM3/PS contents as specified in poly-l–treated cells (in the text) after 45 min of incubation with AVNs. At least 200 cells per condition were imaged. (*D*) Radial distribution functions [g(r)] of PO4 (phosphate group) bead of PS head groups (green), PO4 bead of DPPC and ROH (hydroxyl group) bead of cholesterol head groups (labeled as "GM3-PC," black), and Na^{+} (blue), with GM1 bead of GM3, in CG simulations. (*Inset*) g(r) of P atoms of PS head groups (green), P atoms of DPPC and O atoms of cholesterol head groups (labeled as "GM3-PC," black), and Na^{+} (blue), with heavy atoms of GM3 carbohydrate groups, in AA simulations. Thick lines represent the DPPC:DOPS:cholesterol (CHOL):GM3 (47:10:40:3) system, and the dotted lines represent the control [DPPC:CHOL:GM3 (57:40:3)] membrane, with SDs shaded around the plotted lines. (*E*) Side view of the entire membrane and top view of the membrane head group plane (indicated by the dotted square) of the final configuration after 8 μs CG simulation of the DPPC:DOPS:CHOL:GM3 (47:10:40:3) system. A close-up view of the final configuration of the 1.2 μs AA system is included as *Inset*. Membrane components are rendered in space-filled spherical representation with the color coding of purple (GM3), green (DOPS), gray (DPPC and cholesterol), blue (Na^{+}), yellow (Cl^{−}), and cyan [water (TIP3P)]. (*F*) Quantification of the effect of NaCl on recombinant CD169 binding to AVN through ELISA. The graph plots the relative absorbance (normalized by the absorbance of the respective AVNs in NaCl-free Hepes buffer) for 3/10 and 3/0 AVNs in 1× PBS and 150 mM NaCl. The data are averages of five independent experiments per condition. NS, not significant. ***$P < 0.001$ relative to Hepes measurement.

GM3-CD169 binding. We measured the binding of recombinant CD169 to surface-immobilized GM3-presenting AVNs in NaCl-free Hepes as well as in 1× PBS and 150 mM NaCl. Recombinant CD169 contained a His tag, which was used for quantification via ELISA. For 3/10 AVNs, soluble CD169 binding drops significantly if an Na^{+}-free Hepes buffer is exchanged with 1× PBS or 150 mM NaCl (Fig. 2*F*). In contrast, for 3/0 AVNs, the measured change was not significant. Based on these experimental and simulation-derived findings, we propose that Na^{+}-mediated colocalization of the negatively charged GM3 and PS head groups interferes with the recognition of the lipids through their cellular receptors and effectively reduces the avidity of AVNs containing both GM3 and PS.

Independent of the exact molecular mechanism underlying the GM3-PS antagonism, our results show that the intracellular AVN distribution can be switched between *PH1* and *PH2* by

means of the GM3/PS ratio. We applied focused ion beam SEM (FIB-SEM) (47) used previously by us and others to determine HIV-1 localization in CD169^{+} HeLa cells and mature MDDCs (11, 48) for characterization of the intracellular NP distribution in CD169^{+} macrophages with higher spatial resolution than is possible with confocal optical microscopy. Ion beam milling was used to gradually remove cellular material and facilitate the acquisition of SEM images at different cell depths. Fig. 3*A* shows SEM images for macrophages incubated with either 3/0 AVNs or 3/10 AVNs for 45 min after different milling times between 5 and 155 s. For 3/0 AVNs (GM3-mediated uptake), NP clusters are detectable only during the first 95 s of ion milling, whereas in the case of 3/10 AVNs (PS-mediated uptake), individual NPs are detected at all time points. We conclude that, while 3/10 AVNs remain, to a large extent, monomeric and are diffusively distributed

Fig. 3. Intracellular fates and distributions differ for 3/0 and 3/10 AVNs. (*A*) FIB-SEM images recorded 45 min after AVN addition (*Top* and *Middle*, 3/0 AVNs; *Bottom*, 3/10 AVNs). The images show the same CD169^{+} THP-1 cells at different stages of excavation through focused ion beam milling (specified as depth of milling). *Top* and *Middle* contain 3/0 AVNs; *Bottom* contains 3/10 AVNs. AVNs are marked by red arrows; 3/0 AVNs are primarily found as clusters at the cell periphery, while monomeric 3/10 AVNs are found throughout the cytoplasm. (Scale bars: 2 μm.) (*B*) Scatterplot of normalized intensity as a function of fitted peak wavelength for six randomly selected 3/0 and 3/10 AVN emitters in CD169^{+} THP-1 cells at 5 and 45 min after AVN exposure. A significant spectral red shift is observed for the 3/0 AVN group but not for the 3/10 AVN group after 45 min of incubation. (*C*) Confocal section of CD169^{+} THP-1 cells incubated with 3/0 AVNs (*Upper*) and 3/10 AVNs (*Lower*) for 16 h and immunolabeled for LAMP-1. Rhodamin 6g (Rhg), Alexa647, and DAPI channels are color coded as specified. For the entire cell population, the colocalization rates between AVN and LAMP-1 were 23% for 3/0 and 64% for 3/10. At least 100 cells per condition were imaged. (Scale bars: 5 μm.)

throughout the cytoplasm, 3/0 AVNs are preferentially collected as clusters close to the plasma membrane. Different NP clustering levels for *PH1* and *PH2* are corroborated by spectral shifts in the plasmon resonance of the gold NP labels. The resonance wavelength of gold NP depends on their clustering (49, 50) and thus, provides information about their spatial compartmentalization during trafficking (36, 51, 52). The dark-field spectra of discrete AVNs recorded after 5 and 45 min (Fig. 3*B* and *SI Appendix*, Fig. S3) show a characteristic spectral red shift and broadening for 3/0 AVNs but not for 3/10 AVNs. The red shift observed for 3/0 AVNs signifies a collection of AVNs in subdiffraction limit clusters at the cell periphery, whereas in the case of 3/10 AVNs, the endocytosed NPs remain essentially monomeric over the investigated time range of 45 min. To probe the final intracellular fate of 3/0 and 3/10 AVNs, we mapped their spatial distribution after 16 h. In Fig. 3*C*, we show confocal sections of 3/0 (Fig. 3*C*, *Upper*) and 3/10 (Fig. 3*C*, *Lower*) AVNs. We also performed immunolabeling to detect the intracellular distribution of the lysosomal-associated membrane protein 1 (LAMP-1) to check for putative colocalization of AVNs with lysosomes. The confocal scans reveal that, after 16 h, the 3/0 AVNs are no longer exclusively located at the cell periphery but can also be found in the cell interior. However, the 3/0 AVNs

colocalize poorly with the lysosome, with a colocalization rate around 23%. We conclude that, although the 3/0 AVNs eventually detach from the cell periphery, they do not enter a lysosomal degradation pathway. In contrast, 64% of the 3/10 AVN endocytosed particles are located in cellular compartments that costain with LAMP-1.

The pronounced differences in the spatiotemporal distribution and intracellular fate between 3/0 and 3/10 AVNs highlight that 3/0 AVNs are internalized through a unique pathway that avoids lysosomal compartments. It has recently been shown that CD169 mediates the formation of VCCs (13), which are nonendolysosomal intracellular compartments in macrophages. We hypothesized that 3/0 AVNs captured by CD169 in a GM3-dependent manner induce the formation of VCCs to account for their nonendolysomal intracellular fate. To test this hypothesis, we systematically probed for optical colocalization between 3/0 AVNs and VCC markers, such as tetherin or the tetraspanin CD9 (47). In Fig. 4, we inspect the colocalization between CD9 or tetherin and 3/0 or 3/10 AVNs, respectively, by confocal microscopy. All images were acquired 16 h after AVN addition. Both CD9 and tetherin colocalize with 3/0 AVNs but not 3/10 AVNs, with colocalization efficiencies of 72 and 8% (CD9) as well as 73 and 16% (tetherin) for 3/0 and 3/10

AVNs, respectively. The confocal images confirm the trend from Fig. 3C that, although some 3/0 AVNs are still localized near the plasma membrane, a significant fraction of AVNs has translocated into the cell interior. Importantly, based on their CD9 and tetherin costaining, the 3/0 AVNs containing compartments located at the membrane or in the cell interior identify as VCCs (13, 53). For completeness, we add that the AVNs were stable in THP-1/CD169$^+$ macrophages for times greater than 16 h and that no indications of degradation of AVNs were observed. Even after an incubation time of 48 h, 3/0 AVNs costain with CD9, and 3/10 AVNs costain with LAMP-1 (*SI Appendix*, Fig. S4).

Although our studies were mainly performed with PMA-treated THP-1 cells, which are a commonly used model for monocyte-derived macrophages (MDMs), we validated these findings with patient-derived primary MDMs (*SI Appendix*, Fig. S5). We found that CD9 colocalizes with AVNs in the cell interior of the primary MDMs for a GM3/PS ratio of 3/0 but not for 3/10. For the latter, CD9 remains located at the cell periphery. Conversely, 3/10 AVNs colocalize with LAMP-1, while 3/0 AVNs do not. These CD9 LAMP-1 staining patterns are overall consistent with the behavior observed for THP-1/PMA cells in Fig. 4.

Spearman and coworkers (13) have shown recently that GM3-presenting exogenous HIV-1 Gag VLPs colocalize with HIV-1 in the VCCs of infected MDMs. We, therefore, tested whether GM3-presenting AVNs can successfully mimic the behavior of HIV-1 Gag VLPs. To that end, we first incubated CD169$^+$ THP-1 cells with HIV-1 Gag VLPs for 1 h and then added 3/0 GM3/PS AVNs to challenge the cells for another 1 h. After that, extra VLPs and AVNs were washed away, and the cells were imaged after another 16 h of coincubation. In Fig. 5A, we inspect the colocalization between 3/0 AVNs and HIV VLPs in a representative confocal section. The images unveil an almost indistinguishable spatial distribution between HIV VLPs and 3/0 AVNs after they enter CD169$^+$ THP-1 cells. Regions of intracellular 3/0 AVN and HIV VLP enrichment strongly colocalize with each other. The obvious colocalization between HIV-1 VLPs and 3/0 AVNs in this confocal section not only further illustrates that 3/0 AVNs enter CD169$^+$

THP-1 cells through the VCC pathway but also, provides strong experimental evidence that AVNs and VLPs trigger identical cellular uptake mechanisms.

In the next step, we investigated whether 3/10 AVNs that—due to their high PS content—are not sequestered in VCCs but instead, enter the endolysosomal uptake pathway colocalize with virus particles that are known to utilize PS-mediated binding to host cells. To that end, we chose Ebola VLPs as a test case (54). In Fig. 5B, we map the spatial distribution of 3/10 AVNs, Ebola VLPs, lysosome marker (LAMP-1), and VCC marker (CD9) after 16 h of coincubation. Fig. 5 shows an unambiguous colocalization between 3/10 AVNs and Ebola VLPs. Both 3/10 AVNs and Ebola VLPs colocalize with LAMP-1 but not CD9. Together, the colocalization patterns confirm that AVNs with high PS content and Ebola VLPs are both collected in the lysosome. Importantly, the results show that, by variation of the GM3/PS content in the AVN, membrane intracellular trafficking and destination of either HIV VLPs or Ebola VLPs can be mimicked. The difference in the intracellular fate depends only on the chosen GM3/PS ratio. We mention for completeness that HIV-1 VLPs coincubated with 3/10 AVNs or Ebola VLPs with 3/0 AVN did not show significant colocalizations between AVNs and VLPs (*SI Appendix*, Fig. S6).

Our minimalistic AVN virus model that comprises only four lipid components (phosphatidylcholine, PS, GM3, and cholesterol) confirms that the formation of VCCs is GM3 mediated. One important remaining question is whether the AVN collection in VCCs is unique to GM3-CD169 recognition or whether other gangliosides achieve the same sequestration in VCCs. To address this important question, we assembled 3/0 AVNs, in which we replaced GM3 with GM1. GM1 is structurally related to GM3 and also contains a terminal branched sialic acid residue that binds CD169. The sugar unit in the head group is, however, two units longer for GM1 than for GM3. Despite GM1's ability to bind to CD169 (8, 55), AVNs with a membrane containing 3 mol % GM1 and 0 mol % PS failed to localize to VCCs. Instead, GM1-presenting AVNs were collected in the lysosome after 16 h, and the GM1-containing AVNs show no
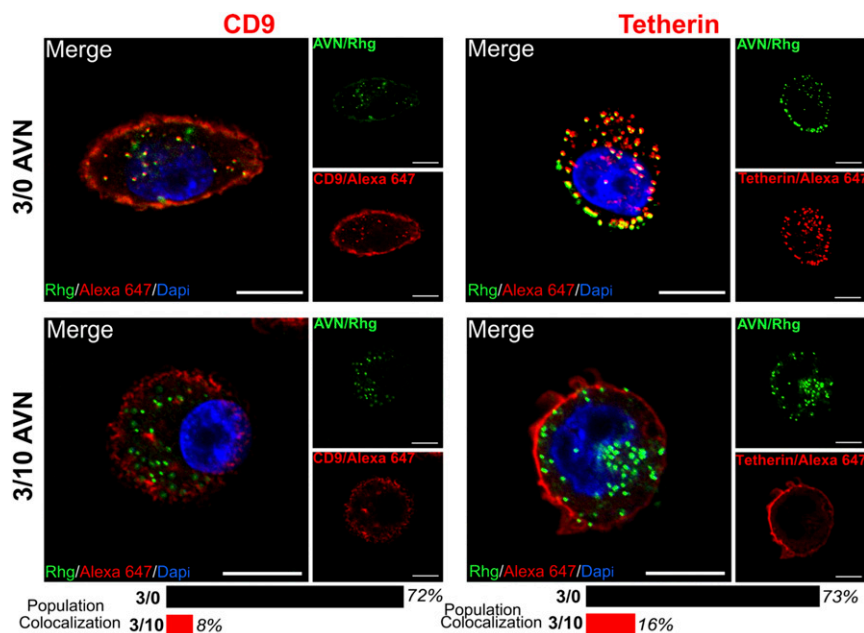

Fig. 4. 3/0 AVNs but not 3/10 AVNs colocalize with VCC markers. (*Left*) Confocal sections of CD169$^+$ THP-1 cells stained for CD9 and containing 3/0 AVNs (*Upper*) and 3/10 AVNs (*Lower*). Images were acquired 16 h after AVN addition. For the entire cell population, the colocalization rates for AVN and CD9 were 72% in the case of 3/0 and 8% for 3/10. (*Right*) Confocal sections stained for tetherin and containing 3/0 AVNs (*Upper*) and 3/10 AVNs (*Lower*). For the entire population, the colocalization rates for AVN and tetherin were 73% in the case of 3/0 and 16% for 3/10. At least 100 cells per condition were imaged. Rhg, Rhodamin 6g channel. (Scale bars: 5 μm.)
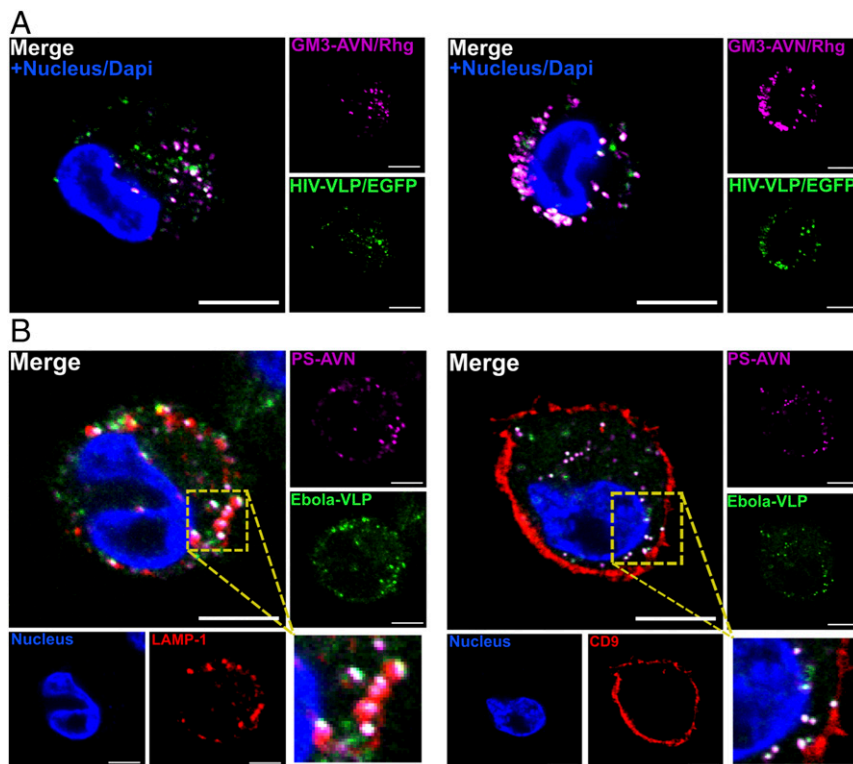
Fig. 5. The 3/0 GM3 AVNs and HIV-1 Gag VLPs colocalize in VCCs, while the 3/10 AVNs and Ebola VLPs are collected in lysosomes. (*A*) AVNs and VLPs show a high degree of spatial colocalization in CD169+ THP-1 cells after 16 h of incubation. Two independent cells are shown here. (*B*) Colocalization between Ebola VLPs, 3/10 AVNs, lysosome marker LAMP-1 (*Left*), and VCC marker CD9 (*Right*). Rhg, Rhodamin 6g channel. (Scale bars: 5 μm.)

overlap with the VCC markers CD9 and tetherin (*SI Appendix*, Fig. S7). We conclude that GM1-CD169 recognition allows binding and subsequent uptake into macrophages but that sequestration in VCCs specifically requires GM3-mediated binding to CD169.

Our analysis has, so far, been focused on elucidating how the AVN membrane composition impacts AVN–cell interactions and ignored the role of the NP core in the AVN design. However, other aspects of the AVN can also play an important role. Of particular interest is the role of the core, as the stiffness of the virus particle has been shown to affect HIV infectivity in different stages (56, 57). Intriguingly, in our experiments, conventional liposomes without NP core but identical nominal membrane composition failed to localize to VCCs. As shown in Fig. 6, neither 3/0 liposomes nor 3/10 liposomes colocalize with tetherin. Instead, both enter an endolysosomal uptake pathway as indicated by their colocalization with LAMP-1. The difference between the 3/0 liposome and AVNs suggests that the GM3 and CD169 recognition alone is insufficient to target VCCs in macrophages but that the NP core itself or its function in presenting and organizing the lipids on the NP surface also plays a role in determining the intracellular fate. This finding emphasizes the potential of AVNs with NP cores from different materials as a platform for investigating the impact of core stiffness on HIV infectivity. Future studies addressing a broader range of NP core stiffness, sizes, and shapes may clarify the role of the core in determining lipid-mediated AVN–cell interactions with primary macrophages and dendritic cells.

Discussion

Our studies have shown that the GM3/PS ratio is key in determining the intracellular fate of AVNs within macrophages. AVNs that present GM3 but not PS are first collected in clusters in a CD169-dependent manner close to the cell periphery. From here, GM3-presenting AVNs gradually translocate into non-

endolysosomal compartments that are enriched in tetherin and tetraspanin CD9, both of which are markers of VCCs (13, 47, 53). This distribution is consistent with an induction of VCC formation by GM3-presenting AVNs. Intriguingly, for AVN-presenting GM1 instead of GM3, we did not detect significant colocalization with VCC markers, suggesting a sensitive dependence of the AVN intracellular fate on the exact molecular structure of the sialic acid-containing head group. Addition of PS to GM3-containing AVN membrane prevents VCC targeting of AVNs and directs the AVNs toward the endolysosomal trafficking pathway. The different intracellular distributions observed for different GM3/PS ratios validate the hypothesis that the membrane composition represents an important regulatory mechanism that determines the intracellular fate of AVNs. Of particular note is the finding that AVNs containing both PS and GM3 show lower binding to CD169-expressing macrophages than AVNs that contain only GM3 or PS. The HIV-1 lipidome is enriched in both PS and GM3, and the 3/10 AVN is, consequently, a realistic virus mimic. The reduced macrophage binding observed experimentally for this GM3/PS ratio raises the question of the biological meaning of the detected antagonism between the two lipids. Ever since the pioneering studies by Adam and Delbruck (58) on 2D confined diffusion in the late 1960s, it is clear that weak binding interactions during initial contact offer advantages for viruses. For one, the weak binding allows the virus to scan different target cells (as opposed to irreversibly sticking to the first encounter), which greatly improves the probability of finding the ideal host cell. Furthermore, weak initial binding interactions allow the virus to explore the cell envelope of the target cell by forming and reforming tethering bonds until it has found the ideal location for penetration (59). In the case of HIV-1, a reduction in lipid-mediated avidity could be advantageous to allow viral glycoproteins to find their binding
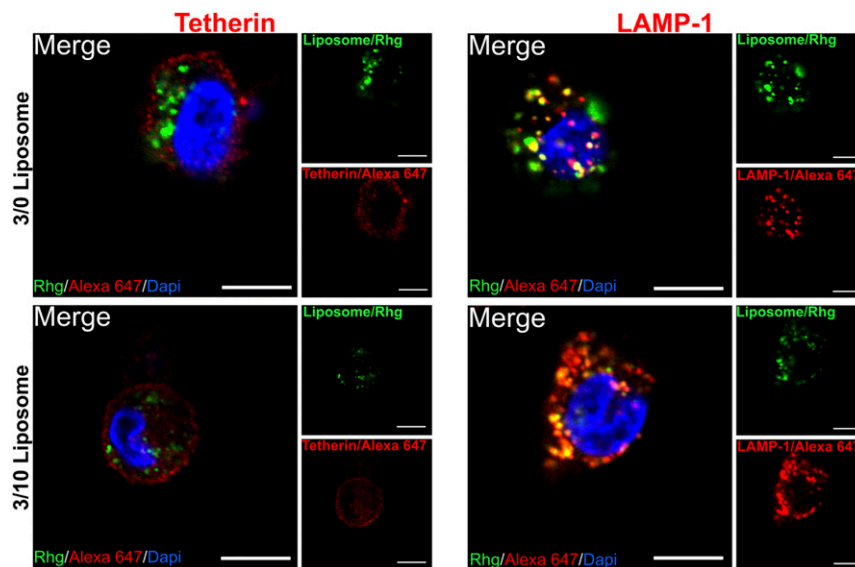
Fig. 6. The 3/0 and 3/10 liposomes enter an endolysosomal pathway. (*Left*) Confocal section containing 3/0 (*Upper*) and 3/10 (*Lower*) liposomes and immunolabeled for tetherin. The image was acquired 16 h after liposome addition. (*Right*) Confocal section containing 3/0 (*Upper*) and 3/10 (*Lower*) liposomes and immunolabeled for LAMP-1 under otherwise identical conditions. Rhg, Rhodamin 6g channel. (Scale bars: 5 μm.)

partner on the host cell surface after an initial lipid-mediated transient contact is established.

A clue into the mechanism that gives rise to the antagonistic behavior between GM3 and PS is offered by the performed MD simulations. The simulations reveal Na$^+$-mediated colocalization between GM3 and PS contained in the AVN membrane, with potential consequences for GM3 recognition through CD169. Experimental binding studies confirmed that—depending on the PS content in the membrane—GM3 binding to CD169 is affected by the Na$^+$ ion concentration. For GM3-presenting AVNs containing high membrane concentrations of PS, Na$^+$ ions decreased the binding of GM3 to solubilized CD169, whereas for GM3-presenting AVNs without PS, no significant difference in binding in the presence or absence of Na$^+$ was detected. One possible explanation for the observed switch in the intracellular fate as a function of increasing GM3/PS ratio is, thus, the perturbation of the GM3-CD169–mediated uptake due to Na$^+$ ion-mediated interactions between GM3 and PS in the AVN membrane. In the presence of an excess of PS, the GM3-mediated mechanism is impeded, and the AVNs enter instead through a PS-mediated uptake pathway.

The observation that 3/0 AVNs are trafficked to VCCs in CD169$^+$ THP-1 cells is particularly relevant in the context of the findings by Spearman and coworkers (13) that GM3-presenting HIV VLPs access HIV-1–containing VCCs in infected cells. The results of this work suggest that AVNs can "switch" their uptake and trafficking patterns to achieve colocalization with HIV VLPs in VCCs or with Ebola VLPs in lysosomes depending on the GM3/PS ratio of the membrane. The finding that the membrane composition can alter the entry pathway in viral glycoprotein-independent virus uptake implies that viral mechanisms aimed at modifying viral membrane composition [for instance, via HIV-1 Gag (60) and Nef (61) proteins] could function to allow the virus switch between different uptake pathways. Nef, for instance, is known to impact the viral lipidome (61), particularly the cholesterol content (62). Since GM3 is enriched in cholesterol-rich plasma membrane microdomains (63), Nef-induced changes in the cholesterol content could indirectly impact GM3 clustering. Although a recent study investigating HIV-1 particles produced in SERINC5-expressing 293T cells has questioned whether changes in the viral lipidome play a role in SERINC5-mediated infectivity restriction and Nef antagonism (64), the virus particles derived from macrophages as

studied in this work may have a different lipid composition. Furthermore, Gag myristoylation controls virus assembly sites (65). As these sites can differ in their composition, Gag myristoylation provides an additional mechanism for modulation of the viral lipidome. The potential for targeting specific viral entry mechanisms through changes in the viral envelope composition via mechanisms that are subject to viral control warrants additional investigation. The AVN platform seems to be uniquely suited to explore and exploit these mechanisms. AVNs are assembled from well-controlled building blocks and can be generated in sterile conditions in large quantities without the need of any cellular expression systems. Although some VLP platforms have been implemented with cell-free expression systems (66, 67), the colloidal AVN assembly approach is simple, fast, and efficient and does not require any enzymes. Different from membranes derived from biological sources, the composition of the AVN membrane is completely determined and can be controlled through choice of the assembly conditions. This compositional control is extremely helpful for investigating specific lipid–receptor interactions. AVNs are protein free, which reduces the risk of a strong immune system response. The latter can be a concern for protein-based VLPs. Furthermore, the AVN approach is compatible with a broad range of engineered NP cores and can provide large contrast in different (fluorescence, MRI, acoustic) imaging modalities depending on the exact choice of the core material. AVNs represent imaging probes that offer a high degree of imaging versatility and brightness that is challenging to match with VLPs. The applicability of AVNs is, however, not limited to that of an imaging probe. It is conceivable to assemble AVNs with a core that can be loaded with pharmaceutical compounds, converting the AVN into a potent lipid-guided delivery vehicle. The findings of this study suggest that GM3-presenting AVNs provide a platform for selectively targeting VCC-associated HIV-1 reservoirs and encourage future in vivo studies to evaluate the possibility of eradicating this reservoir with AVN-formulated antiretroviral drugs.

Materials and Methods

Liposome and AVN Preparation. A total amount of 1 μmol of lipid mix containing DPPC, cholesterol, DOPS, GM3 Ganglioside (milk, bovine ammonium salt; GM3), and the fluorescence marker 1,2-dipalmitoyl-*sn*-glycero-3-phosphoethanolamine-*N*-(lissamine rhodamine B sulfonyl) (ammonium salt; Avanti Polar Lipids) was dissolved in around 100 μL chloroform in a 25-mL round-bottom flask. The contributions from the individual lipids varied for different

preparations as specified in the text. The solvent was then evaporated, and the samples were dried overnight in a vacuum rotary evaporator; 1 mL of 20 mM Hepes buffer (pH 7.2; Sigma-Aldrich) was then added to the lipid dry layer, forming a cloudy solution after vigorous agitation. The mixture was then probe sonicated (Fisher Scientific model 120 Sonic Dismembrator, 50/60 Hz) for 3–5 min under argon protection until the solution became clear. The resulting liposome solution was stored at 4 °C until further use; 1 mL of 90 nm citrate-stabilized gold colloid solution (~1.0×10^{10} particles per 1 mL), synthesized following the Turkevich method as previously described (10, 11, 29), was pelleted via centrifugation at $600 \times g$ for 10 min. A volume of 0.5 mL of the prepared liposome solution was added to the gold NP pellet. The volume was increased to 1 mL with the same 20 mM Hepes buffer. A volume of 20 μL of 1 mg/mL 1-octadecanethiol solution in ethanol was then added to the mixture. The mixed solution was incubated overnight on a rocker. After that, the AVNs were washed three times through centrifugation ($600 \times g$, 10 min) and resuspended in Milli-Q water. Finally, the AVN pellet was resuspended in 200 μL 20 mM Hepes buffer and ready to use.

Ganglioside GM1 ELISA. Relative GM1 loadings on AVN were quantified through a tetramethylbenzidine (TMB)-based sandwich ELISA kit in a polylysine-coated 96-well plate. The individual wells were incubated with AVNs for 1 h. After that, the AVN solution was retrieved from the wells. We determined the AVN concentration before and after loading of the wells through ultraviolet-visible spectroscopy, and the difference in the number of AVNs was assumed to be bound to the wells. After thoroughly washing each well with washing buffer (Thermo Fisher Scientific), 200 μL of a 100 ng/mL rabbit polyclonal anti-GM1 antibody (abcam) in 1× PBS containing 0.1 mg/mL BSA (Sigma-Aldrich) was incubated in the wells for 2 h at room temperature. Excess antibodies were then removed by washing three times before 200 μL of a 10 ng/mL goat anti-rabbit IgG HRP-conjugated antibody (abcam) solution (1× PBS with 0.1 mg/mL BSA) was added into each well and incubated for 1 h. After washing three times, 0.5 mM TMB solution was added into each well and incubated for 30 min before a stop solution was added. The plate was then read out using an excitation wavelength of 450 nm. The measured absorbance was normalized by the bound AVN signal and corrected by the absorbance of a blank AVN control (no GM1).

Measuring Recombinant CD169 Binding to Surface-Immobilized AVN. AVN were bound to a polylysine-coated 96-well plate. After extensive washing of the wells with washing buffer (Thermo Fisher Scientific), 50 μL of a 1 μg/mL solution of CD169 with C-terminal 6-His tag (R&D systems) in Hepes, 1× PBS, or 150 mM NaCl was incubated in the wells for 1 h. The CD169 solutions were obtained by diluting a 100 μg/mL solution of recombinant protein in 1× PBS with the buffer of choice. After washing three times, 50 μL of anti-His tag rabbit antibody (abcam) was added at a concentration of 1 μg/mL in 1× PBS containing 0.1 mg/mL BSA and incubated for another 1 h. The wells were washed three times before 50 μL of a 10 ng/mL goat anti-rabbit IgG HRP-conjugated antibody solution (1× PBS with 0.1 mg/mL BSA) was added and incubated for 1 h. Finally, after washing three times, a 0.5 mM TMB solution was added into each well and incubated for 30 min before a stop solution was added. The plate was then read out using an excitation wavelength of 450 nm. The measured absorbance was corrected by the signal from an empty well.

Dynamic Light Scattering and Zeta Potential Measurements. Measurements were performed on a Zetasizer Nano ZS90. For size measurements, AVNs were diluted with Milli-Q water to a final concentration of 1×10^8 particles per 1 mL For zeta measurements, the AVN samples were further diluted to 1×10^7 particles per 1 mL Measured zeta potentials were converted into surface charge densities using the Grahame equation.

Cell Culture. THP-1/CD169 cells (CD169$^+$ THP-1) have been described previously (14). CD169$^+$ THP-1 cells were cultured in 10% FBS, 1% penicillin–streptomycin, and 2% G418 in RPMI-1640 medium (Gibco Cell Culture; Thermo Fisher Scientific). CD169$^+$ THP-1 cells were differentiated into macrophages by incubation with 100 nM PMA (Sigma-Aldrich) for 48 h. Human MDMs were differentiated from positively isolated CD14$^+$ peripheral blood monocytes by culturing in RPMI-1640 containing 10% heat-inactivated human AB serum (Sigma-Aldrich) and recombinant human macrophage colony stimulating factor (20 ng/mL; PeproTech) for 5–6 d (38).

VLP Generation. HIV Gag-EGFP VLPs and Ebola EGFP-VP40 VLPs were produced via transfection of HEK293T cells as described previously (60).

AVN Administration and Cell Staining. AVNs with a predetermined GM3/PS ratio were incubated with CD169$^+$ THP-1 cells at a concentration of 1×10^7/mL (1,000 AVNs per cell) for 5 or 45 min, as specified, in FBS-free RPMI-1640 medium. The unbound AVNs were then removed, and the cells were washed and fixed for inspection in the optical microscope. In some experiments, the cells were subsequently lysed to determine the average gold content per cell by ICP-MS. For the 16-h experiment, cells were washed with warm RPMI-1640 medium after 45 min of incubation with AVNs and then maintained in the CO$_2$ incubator for another ~16 h in complete medium. Cells were fixed with 4% paraformaldehyde (Sigma-Aldrich), permeabilized with 0.2% Tween-20 (Sigma-Aldrich), and blocked with 1% BSA. Then, cells were stained with CD9 mAb, CD107a mAb, and CD-137 mAb (BioLegend) to probe CD9, LAMP-1, and Tetherin, respectively, and detected with Alexa647-conjugated secondary antibody (BioLegend). A typical antibody concentration was 1 μg/mL.

ICP-MS. Cells were washed three times with warm 1× PBS buffer and harvested using a cell dissociation buffer (Gibco; Thermo Fisher Scientific). After that, the cells were transferred into centrifuge tubes. Excess particles and cells were separated by centrifugation three times at $40 \times g$ for 5 min and subsequent resuspension in 1× PBS. The cell concentration was then measured with a flow cytometer. Cell samples of known concentration were transferred into a 12-well dish, and fresh aqua regia was added to the wells to dissolve cells and the contained gold NP. The dish was then placed on top of a hot plate preset to 55 °C overnight to evaporate the aqua regia. The dried sample was redispersed in 2% HCl solution and measured together with defined calibration standards in VG Plasma Quad ExCell ICP-MS to determine the gold concentration in the sample. The concentration of gold per cell was calculated by dividing the measured gold content by the number of cells.

FIB-SEM. Cells intended for FIB-SEM sectioning were first cultured on a 0.01 vol % polylysine (Sigma-Aldrich)-pretreated 1×1-cm Si chip and exposed to AVNs as described above. Cells were then fixed in 4% paraformaldehyde and 1% glutaraldehyde in 0.1 M sodium cacodylate buffer (pH 7.2) for 15 min at room temperature. After that, the samples were incubated with 1% osmium tetroxide in distilled water for 30 min. Subsequently, samples were washed with distilled water and then dried with 50, 75, 95, and 100% ethanol solutions, and finally, they were placed in Hexamethyldisilazane overnight. Samples were imaged first using a Zeiss Supra 40VP SEM at 2.0 kV and a working distance of 10 mm. The samples were subsequently milled with an FEI Quanta 3D FIB instrument using a voltage of 30.0 kV and a current of 0.5 nA for the specified time durations.

Image Acquisition and Data Processing. All optical imaging experiments were performed with either an Olympus IX71 inverted wide-field microscope or an Olympus FV1000 scanning confocal microscope. The gold NP signal was collected through confocal backscattering measurements. For images taken on the wide-field microscopes, a 60× oil objective with variable N.A. (N.A. = 0.65–1.25) was used. For dark-field imaging, the samples were illuminated with a 100-W tungsten lamp through a high-N.A. oil dark-field condenser (N.A. = 1.2–1.4). Dark-field images were recorded with a Nikon D3100 SLR digital camera connected to the microscope through an eyepiece adaptor. Fluorescence imaging was performed under epiillumination using appropriate filter sets with a mercury lamp. Images were recorded with an Andor Ixon+ electron multiplying CCD detector. For images taken on the confocal microscope, a series of 10×, 20×, 40×, and 60× (water) objectives was used to localize the field of interest. Confocal fluorescence images were recorded using different excitation wavelengths (405, 488, and 633 nm) as needed for the applied dyes. All recorded images by wide-field and confocal microscopes were further processed by ImageJ for coordinate alignment, overlay, and generating pseudocolors.

1. Callahan MK, et al. (2003) Phosphatidylserine on HIV envelope is a cofactor for infection of monocytic cells. *J Immunol* 170:4840–4845.
2. Amara A, Mercer J (2015) Viral apoptotic mimicry. *Nat Rev Microbiol* 13:461–469.
3. Jemieliy S, et al. (2013) TIM-family proteins promote infection of multiple enveloped viruses through virion-associated phosphatidylserine. *PLoS Pathog* 9:e1003232.
4. Mercer J, Helenius A (2008) Vaccinia virus uses macropinocytosis and apoptotic mimicry to enter host cells. *Science* 320:531–535.
5. Mercer J, Schelhaas M, Helenius A (2010) Virus entry by endocytosis. *Annu Rev Biochem* 79:803–833.
6. Izquierdo-Useros N, et al. (2010) HIV and mature dendritic cells: Trojan exosomes riding the Trojan horse? *PLoS Pathog* 6:e1000740.
7. Izquierdo-Useros N, et al. (2014) HIV-1 capture and transmission by dendritic cells: The role of viral glycolipids and the cellular receptor Siglec-1. *PLoS Pathog* 10: e1004146.

CHEMISTRY

MICROBIOLOGY

8. Puryear WB, Yu X, Ramirez NP, Reinhard BM, Gummuluru S (2012) HIV-1 incorporation of host-cell-derived glycosphingolipid GM3 allows for capture by mature dendritic cells. *Proc Natl Acad Sci USA* 109:7475–7480.

9. Puryear WB, et al. (2013) Interferon-inducible mechanism of dendritic cell-mediated HIV-1 dissemination is dependent on Siglec-1/CD169. *PLoS Pathog* 9:e1003291.

10. Yu X, et al. (2015) Dressing up nanoparticles: A membrane wrap to induce formation of the virological synapse. *ACS Nano* 9:4182–4192.

11. Yu X, et al. (2014) Glycosphingolipid-functionalized nanoparticles recapitulate CD169-dependent HIV-1 uptake and trafficking in dendritic cells. *Nat Commun* 5:4136.

12. Kijewski SD, Gummuluru S (2015) A mechanistic overview of dendritic cell-mediated HIV-1 *trans* infection: The story so far. *Future Virol* 10:257–269.

13. Hammonds JE, et al. (2017) Siglec-1 initiates formation of the virus-containing compartment and enhances macrophage-to-T cell transmission of HIV-1. *PLoS Pathog* 13:e1006181.

14. Akiyama H, Ramirez N-GP, Gudheti MV, Gummuluru S (2015) CD169-mediated trafficking of HIV to plasma membrane invaginations in dendritic cells attenuates efficacy of anti-gp120 broadly neutralizing antibodies. *PLoS Pathog* 11:e1004751.

15. Tan J, Sattentau QJ (2013) The HIV-1-containing macrophage compartment: A perfect cellular niche? *Trends Microbiol* 21:405–412.

16. Graziano F, et al. (2015) Extracellular ATP induces the rapid release of HIV-1 from virus containing compartments of human macrophages. *Proc Natl Acad Sci USA* 112:E3265–E3273.

17. Pierson T, McArthur J, Siliciano RF (2000) Reservoirs for HIV-1: Mechanisms for viral persistence in the presence of antiviral immune responses and antiretroviral therapy. *Annu Rev Immunol* 18:665–708.

18. Josefsson L, et al. (2013) The HIV-1 reservoir in eight patients on long-term suppressive antiretroviral therapy is stable with few genetic changes over time. *Proc Natl Acad Sci USA* 110:E4987–E4996.

19. Brügger B, et al. (2006) The HIV lipidome: A raft with an unusual composition. *Proc Natl Acad Sci USA* 103:2641–2646.

20. Shi X, et al. (2007) Dendrimer-entrapped gold nanoparticles as a platform for cancer-cell targeting and imaging. *Small* 3:1245–1252.

21. Shi X, Wang S, Sun H, Baker JR (2007) Improved biocompatibility of surface functionalized dendrimer-entrapped gold nanoparticles. *Soft Matter* 3:71–74.

22. Kroll AV, Fang RH, Zhang L (2017) Biointerfacing and applications of cell membrane-coated nanoparticles. *Bioconjug Chem* 28:23–32.

23. Mamo T, et al. (2010) Emerging nanotechnology approaches for HIV/AIDS treatment and prevention. *Nanomedicine (Lond)* 5:269–285.

24. Tarn D, et al. (2013) Mesoporous silica nanoparticle nanocarriers: Biofunctionality and biocompatibility. *Acc Chem Res* 46:792–801.

25. Yang JA, Murphy CJ (2012) Evidence for patchy lipid layers on gold nanoparticle surfaces. *Langmuir* 28:5404–5416.

26. Fang RH, et al. (2014) Cancer cell membrane-coated nanoparticles for anticancer vaccination and drug delivery. *Nano Lett* 14:2181–2188.

27. van Schooneveld MM, et al. (2008) Improved biocompatibility and pharmacokinetics of silica nanoparticles by means of a lipid coating: A multimodality investigation. *Nano Lett* 8:2517–2525.

28. Liu J, Stace-Naughton A, Jiang X, Brinker CJ (2009) Porous nanoparticle supported lipid bilayers (protocells) as delivery vehicles. *J Am Chem Soc* 131:1354–1355.

29. Xu F, et al. (2016) Lipid-mediated targeting with membrane-wrapped nanoparticles in the presence of corona formation. *ACS Nano* 10:1189–1200.

30. Melby ES, et al. (2016) Formation of supported lipid bilayers containing phase-segregated domains and their interaction with gold nanoparticles. *Environ Sci Nano* 3:45–55.

31. Yang JA, Lohse SE, Murphy CJ (2014) Tuning cellular response to nanoparticles via surface chemistry and aggregation. *Small* 10:1642–1651.

32. Wang G, Sun W, Luo Y, Fang N (2010) Resolving rotational motions of nano-objects in engineered environments and live cells with gold nanorods and differential interference contrast microscopy. *J Am Chem Soc* 132:16417–16422.

33. Schultz S, Smith DR, Mock JJ, Schultz DA (2000) Single-target molecule detection with nonbleaching multicolor optical immunolabels. *Proc Natl Acad Sci USA* 97:996–1001.

34. Qian W, Huang X, Kang B, El-Sayed MA (2010) Dark-field light scattering imaging of living cancer cell component from birth through division using bioconjugated gold nanoprobes. *J Biomed Opt* 15:046025.

35. Zhang P, Lee S, Yu H, Fang N, Kang SH (2015) Super-resolution of fluorescence-free plasmonic nanoparticles using enhanced dark-field illumination based on wavelength-modulation. *Sci Rep* 5:11447.

36. Wu L, Reinhard BM (2014) Probing subdiffraction limit separations with plasmon coupling microscopy: Concepts and applications. *Chem Soc Rev* 43:3884–3897.

37. Li F, et al. (2010) Detection of *Escherichia coli* O157:H7 using gold nanoparticle labeling and inductively coupled plasma mass spectrometry. *Anal Chem* 82:3399–3403.

38. Akiyama H, et al. (2017) Interferon-inducible CD169/Siglec1 attenuates anti-HIV-1 effects of alpha interferon. *J Virol* 91:e00972-e17.

39. Wong K, et al. (2010) Phosphatidylserine receptor Tim-4 is essential for the maintenance of the homeostatic state of resident peritoneal macrophages. *Proc Natl Acad Sci USA* 107:8712–8717.

40. Borisenko GG, et al. (2003) Macrophage recognition of externalized phosphatidylserine and phagocytosis of apoptotic Jurkat cells–Existence of a threshold. *Arch Biochem Biophys* 413:41–52.

41. Zou Z, et al. (2011) Siglecs facilitate HIV-1 infection of macrophages through adhesion with viral sialic acids. *PLoS One* 6:e24559.

42. Sewald X, et al. (2015) Retroviruses use CD169-mediated trans-infection of permissive lymphocytes to establish infection. *Science* 350:563–567.

43. Lemke G, Rothlin CV (2008) Immunobiology of the TAM receptors. *Nat Rev Immunol* 8:327–336.

44. Freeman GJ, Casasnovas JM, Umetsu DT, DeKruyff RH (2010) *TIM* genes: A family of cell surface phosphatidylserine receptors that regulate innate and adaptive immunity. *Immunol Rev* 235:172–189.

45. Marrink SJ, Tieleman DP (2013) Perspective on the Martini model. *Chem Soc Rev* 42:6801–6822.

46. Schmalhorst PS, Deluweit F, Scherrers R, Heisenberg C-P, Sikora M (2017) Overcoming the limitations of the MARTINI force field in simulations of polysaccharides. *J Chem Theory Comput* 13:5039–5053.

47. Chu H, et al. (2012) Tetherin/BST-2 is essential for the formation of the intracellular virus-containing compartment in HIV-infected macrophages. *Cell Host Microbe* 12:360–372.

48. Felts RL, et al. (2010) 3D visualization of HIV transfer at the virological synapse between dendritic cells and T cells. *Proc Natl Acad Sci USA* 107:13336–13341.

49. Reinhard BM, Siu M, Agarwal H, Alivisatos AP, Liphardt J (2005) Calibration of dynamic molecular rulers based on plasmon coupling between gold nanoparticles. *Nano Lett* 5:2246–2252.

50. Chen T, Pourmand M, Feizpour A, Cushman B, Reinhard BM (2013) Tailoring plasmon coupling in self-assembled one-dimensional Au nanoparticle chains through simultaneous control of size and gap separation. *J Phys Chem Lett* 4:2147–2152.

51. Wang J, Boriskina SV, Wang H, Reinhard BM (2011) Illuminating epidermal growth factor receptor densities on filopodia through plasmon coupling. *ACS Nano* 5:6619–6628.

52. Wang H, Wu L, Reinhard BM (2012) Scavenger receptor mediated endocytosis of silver nanoparticles into J774A.1 macrophages is heterogeneous. *ACS Nano* 6:7122–7132.

53. Chu H, et al. (2012) The intracellular virus-containing compartments in primary human macrophages are largely inaccessible to antibodies and small molecules. *PLoS One* 7:e35297.

54. Yuan S, et al. (2015) TIM-1 acts a dual-attachment receptor for Ebolavirus by interacting directly with viral GP and the PS on the viral envelope. *Protein Cell* 6:814–824.

55. Izquierdo-Useros N, et al. (2012) Sialyllactose in viral membrane gangliosides is a novel molecular recognition pattern for mature dendritic cell capture of HIV-1. *PLoS Biol* 10:e1001315.

56. Ramalho R, Rankovic S, Zhou J, Aiken C, Rousso I (2016) Analysis of the mechanical properties of wild type and hyperstable mutants of the HIV-1 capsid. *Retrovirology* 13:17.

57. Kol N, et al. (2007) A stiffness switch in human immunodeficiency virus. *Biophys J* 92:1777–1783.

58. Adam G, Delbruck M (1968) Reduction of dimensionality in biological diffusion processes. *Structural Chemistry and Molecular Biology*, eds Rich A, Davidson N (Freeman, San Francisco).

59. Ohki S (2012) *Cell and Model Membrane Interactions* (Springer, New York).

60. Akiyama H, et al. (2014) Virus particle release from glycosphingolipid-enriched microdomains is essential for dendritic cell-mediated capture and transfer of HIV-1 and henipavirus. *J Virol* 88:8813–8825.

61. Brügger B, et al. (2007) Human immunodeficiency virus type 1 Nef protein modulates the lipid composition of virions and host cell membrane microdomains. *Retrovirology* 4:70.

62. Zheng Y-H, Plemenitas A, Fielding CJ, Peterlin BM (2003) Nef increases the synthesis of and transports cholesterol to lipid rafts and HIV-1 progeny virions. *Proc Natl Acad Sci USA* 100:8460–8465.

63. Fujita A, et al. (2007) Gangliosides GM1 and GM3 in the living cell membrane form clusters susceptible to cholesterol depletion and chilling. *Mol Biol Cell* 18:2112–2122.

64. Trautz B, et al. (2017) The host-cell restriction factor SERINC5 restricts HIV-1 infectivity without altering the lipid composition and organization of viral particles. *J Biol Chem* 292:13702–13713.

65. Saad JS, et al. (2006) Structural basis for targeting HIV-1 Gag proteins to the plasma membrane for virus assembly. *Proc Natl Acad Sci USA* 103:11364–11369.

66. Rohovie MJ, Nagasawa M, Swartz JR (2017) Virus-like particles: Next-generation nanoparticles for targeted therapeutic delivery. *Bioeng Transl Med* 2:43–57.

67. Bundy BC, Franciszkowicz MJ, Swartz JR (2008) Escherichia coli-based cell-free synthesis of virus-like particles. *Biotechnol Bioeng* 100:28–37.